EWSR1 affects PRDM9-dependent histone 3 methylation and provides a link between recombination hotspots and the chromosome axis

Hui Tian, Timothy Billings, Michael Walker, Pavlina M. Petkova, Christopher L. Baker, Petko M. Petkov*

The Jackson Laboratory, Bar Harbor, ME 04609, USA

*Correspondence and Lead Contact: petko.petkov@jax.org

Abstract

Meiotic recombination in most mammals requires recombination hotspot activation through the action of the histone 3 lysine-4 and lysine-36 methyltransferase PRDM9 to ensure successful double-strand break initiation and repair. Here we show that EWSR1, a protein with a previously uncharacterized role in meiosis, binds to PRDM9 and increases the efficiency of trimethylation at hotspots *in vivo*. Additionally, EWSR1 provides a link between PRDM9-activated hotspots and the nascent chromosome axis through the phosphorylated meiosis-specific cohesin pREC8. Together, these two functions of EWSR1 affect the choice of which hotspots will be used for double-strand break formation and repair, assuring that a sufficient number of crossovers are properly positioned along the centromere-telomere axis. These results show that successful recombination and meiosis require proper association of activated hotspots with the chromosome axis, and that one of the pathways involved in this association is mediated by interactions between EWSR1, PRDM9, and pREC8.

Introduction

Correct genetic recombination during meiosis is required for the production of fertile, euploid gametes and the creation of new combinations of parental alleles (Kleckner 1996; Keeney et al. 1997; Hassold and Hunt 2001). In most mammals, including humans and mice, recombination occurs at defined genomic sites, termed hotspots, whose positions and activity are determined by the meiosis-specific protein PR/SET Domain 9 (PRDM9) (Baudat et al. 2010; Myers et al. 2010; Parvanov et al. 2010). Meiotic recombination initiates at leptonema, the first stage of the prolonged prophase I of meiosis, when PRDM9 binds to hotspot sequences with its zinc finger domain and trimethylates histone 3 at lysine 4 (H3K4me3) and lysine 36 (H3K36me3) with its PR/SET domain (Baudat et al. 2010; Berg et al. 2010; Myers et al. 2010; Parvanov et al. 2010; Powers et al. 2016). Double-stranded DNA breaks (DSBs) then form at some of the activated sites by the action of the topoisomerase-like protein SPO11 (Keeney et al. 1997; Romanienko and Camerini-Otero 1999). The strand bound to SPO11 is then resected (Keeney et al. 1997) and the resulting single-strand ends are used to establish contact between homologous chromosomes (Hunter and Kleckner 2001). The resulting recombination intermediates eventually resolve to form crossovers or non-crossovers, with a strong preference for non-crossovers (Borner et al. 2004; Martini et al. 2011; Tang et al. 2015). The number and positioning of the PRDM9-trimethylated sites, DSBs and crossovers are under stringent control. In C57BL/6J (B6) male mice, it is estimated that ~4,700 hotspots are modified by PRDM9 in an average meiosis (Baker et al. 2014). Of these, only ~200-300 are used for DSB formation (Cole et al. 2012; Kauppi et al. 2013), which are in turn repaired to produce mostly non-crossovers and only 22-24

crossovers (Koehler et al. 2002). This strict regulation of meiotic recombination events at each step is required to ensure accurate progression of meiosis (Hassold and Hunt 2001; Cole et al. 2012). The determination of whether or not a PRDM9 binding site is used for recombination initiation is affected by multiple factors, including allelic competition (Baker et al. 2015a) and local chromatin structure (Walker et al. 2015).

The complexity of the process of meiosis, and the stringent controls in place, strongly suggest the involvement of multiple proteins. Many of the proteins involved in DSB formation and repair are known (Romanienko and Camerini-Otero 1999; Borner et al. 2004; Hunter 2015; Kumar et al. 2015; Robert et al. 2016; Stanzione et al. 2016). However, we have little understanding of how the recombination machinery recognizes PRDM9-activated hotspots, what decides which of these will be chosen for DSB formation, and how DSBs are associated with the chromosome axis elements (Ishiguro et al. 2011). We recently identified Ewing sarcoma RNA binding protein 1 (EWSR1) as a binding partner of PRDM9 during meiotic prophase I through its C-terminal domain, and showed that PRDM9 also interacts with elements of chromosome axis including phosphorylated meiotic cohesin protein REC8 (pREC8) and synaptonemal complex proteins SYCP3 and SYCP1 (Parvanov et al. 2017).

In wild type mice, EWSR1 is expressed in most of tissues and cell types, including both Sertoli cells and germ cells in seminiferous tubules (Parvanov et al. 2017). Systemic knockout of *Ewsr1* in mice results in high postnatal lethality, defects in pre-B cell development, premature cellular senescence, hypersensitivity to ionizing radiation, and sterility in any surviving mice (Li et al. 2007).Therefore, we created a conditional knockout mouse model in which *Ewsr1* is deleted in germ cells at the onset of meiosis

to further evaluate the function of EWSR1 specifically in meiotic recombination. Here we show that EWSR1 plays important roles in at least one recombination initiation pathway, promoting PRDM9-dependent histone methylation at hotspots and providing a physical link between activated hotspots and pREC8-containing meiosis-specific cohesin complexes, thus affecting the subsequent hotspot choices for DSB formation and crossover resolution.

Results

Ewsr1 conditional knockout (CKO) mice are sterile with meiotic arrest

To determine the function of EWSR1 in meiosis, we deleted *Ewsr1* from spermatocytes at the onset of meiosis (before pre-leptonema) using *Stra8-iCre*. In *Ewsr1* conditional knockout (*Ewsr1*$^{loxp/\Delta;Stra8\text{-}iCre}$, hereafter referred to as *Ewsr1* CKO) testis, the EWSR1 signal was absent in spermatocytes only (Fig S1A, arrow in upper panels). Spermatogonia and Sertoli cells were not affected (Fig S1A, arrowhead in upper panels), indicating successful spermatocyte-specific *Ewsr1* deletion. There is a small portion of spermatocytes (<10%) with incomplete EWSR1 excision (Fig S1A, arrow in lower panels).

Ewsr1 CKO mice were sterile, while heterozygous control (*Ewsr1*$^{loxp/+;Stra8\text{-}iCre}$, hereafter referred to as *Ewsr1* control) matings produced a normal number of viable pups (Fig 1A). Loss of *Ewsr1* in spermatocytes led to a significant reduction in testis size compared to controls. The testis weight index was markedly lower in adult CKO than in control mice (Fig 1B), but not in juvenile mice at 14 or 18 days postpartum (dpp) (Fig S1B). Histologically, *Ewsr1* deficiency resulted in loss of spermatocytes in

seminiferous tubules beyond prophase I and loss of post-meiotic germ cells (Fig 1C, upper panels). Consequently, no mature sperm were observed in the CKO epididymis (Fig 1C, lower panels). There was also a marked increase in the number of apoptotic germ cells in CKO compared to control testes (Fig 1D and E).

Meiosis appears blocked at pachynema/diplonema in CKO mice. Although the proportions of late pachytene spermatocytes, marked by H1t (Cobb et al. 1999) (Fig S1C), were reduced in CKO compared to control testes ($p < 0.05$), the proportions of leptotene and zygotene spermatocytes were not significantly different ($p = 0.21$, *Chi-square*; Fig S1D).

We used spermatocyte spreads to examine meiotic progression in CKO testis. First, we examined the formation and repair of DSBs using phosphorylated H2AX (γH2AX) as a marker of unrepaired DNA lesions. In normal meiosis, the γH2AX signal is seen throughout the nucleus in leptotene spermatocytes when DSBs are occurring; as the breaks are repaired, the signal is restricted to the sex body (Mahadevaiah et al. 2001) by pachynema. CKO spermatocytes were similar in that the γH2AX signal was detected normally during leptonema and zygonema, and at pachynema most of the signal was restricted to the sex body (Fig S1E). However, ~24.3% of sex chromosomes were not attached to each other, compared to 0.7% in *Ewsr1* control spermatocytes ($p < 0.05$, Fig 1F, middle panel, and S1E, arrow); in addition, ~8.5% of CKO pachytene spermatocytes showed remained γH2AX signal on autosomes, compared to ~0.9 % in controls ($p < 0.05$). These results suggest asynapsis at autosomes (Fig 1F, right panel, arrow). To further examine the effect of EWSR1 loss on sex body formation and synapsis, we used ATR, BRCA1 and HORMAD1 as markers of sex bodies and unsynapsed chromosome

axes. Round–spread ATR signal covering the sex chromosomes and BRCA1 signal along the XY axes were observed on the sex bodies of both CKO and control pachytene spermatocytes (Fig S1F), but, as with γH2AX staining, more unsynapsed XY chromosomes were observed in CKO (Fig S1F, arrows). HORMAD1 staining also indicated XY chromosomes asynapsis in CKO spermatocytes, with no such asynapsis in control spermatocytes. There was also a marked increase in autosomal asynapsis in CKO compared to control spermatocytes (Fig S1F, arrow).

Together, these results suggest that depletion of EWSR1 in spermatocytes affects normal DSB repair and chromosome synapsis.

PRDM9 and its interactor proteins are expressed normally in the absence of EWSR1

EWSR1 was identified as one of the strongest binding partners of PRDM9 (Parvanov et al. 2017). Therefore, we analyzed whether the loss of EWSR1 in spermatocytes affects the expression and/or localization of PRDM9 and its interactors. PRDM9 expression is normally restricted to the nucleus at leptonema and zygonema (Sun et al. 2015). In the absence of EWSR1, there was no change in PRDM9 expression pattern (Fig 2A, upper two rows) or its protein level (Fig S2A) in 14 dpp CKO spermatocytes. We also found no difference in protein levels of the other PRDM9 interactors we identified previously (Parvanov et al. 2017), including EHMT2 and the chromosome axis proteins REC8 and SYCP3 in CKO testes compared to the controls (Fig S2A), and the pattern of EHMT2 or CDYL localization was the same in spermatogonia and spermatocytes of CKO and controls (Fig S2B).

These data indicate that EWSR1 is not involved in regulating the expression and localization of PRDM9 or its interactors during spermatogenesis.

H3K4 and H3K36 trimethylation levels at hotspots are reduced in the absence of EWSR1

To determine whether EWSR1 participates in the regulation of hotspot activation by PRDM9, we first compared the patterns of H3K4me3 marks in control, CKO, and *Prdm9* knockout (*Prdm9*^{tm1Ymat} (Hayashi et al. 2005), referred to as *Prdm9*$^{-/-}$) testes. Immunostaining of spreads of wild type B6 mice showed abundant H3K4me3 signal present at leptonema and zygonema but very little at pachynema (Fig S3A and (Buard et al. 2009)), a pattern that matches the expression of PRDM9 (Parvanov et al. 2017), while the H3K36me3 signal was detected from leptonema to diplonema as it is present in actively transcribed gene bodies (Fig S3B). In contrast, there was low H3K4me3 signal in both leptonema/zygonema and pachytene-like cells in *Prdm9*$^{-/-}$ spermatocytes (Fig S3A), indicating that the robust H3K4me3 signal in wild type leptonema and zygonema is mostly PRDM9-dependent. Similarly, H3K4me3 and H3K36me3 signal at leptonema and zygonema was reduced in the absence of EWSR1 when compared to controls (Fig 2A, lower two rows and Fig S3B).

To test whether loss of EWSR1 affects the methyltransferase activity of PRDM9 at hotspots, we performed H3K4me3 and H3K36me3 ChIP-seq from 14-dpp testes (Fig S4A). We found 10,898 PRDM9-dependent H3K4me3 peaks in controls, and only 7,571 peaks in CKO spermatocytes (FDR < 0.01, Fig 2B) using the detection criteria described previously (Walker et al. 2015). Over 88.2% of the hotspot peaks in CKO

spermatocytes were present in the controls (6,679 out of 7,571). Conversely, about 38.7% of the hotspot peaks in control spermatocytes (4,219 out of 10,898) were missing in CKO spermatocytes (Fig 2B). The missing hotspots were those that had lower H3K4 trimethylation levels in controls (Fig 2C), and the H3K4me3 levels at the remaining hotspots were reduced (Fig 2D, red points. $p < 2\times10^{-16}$, Wilcoxon rank sum test). In contrast, H3K4 trimethylation at non-hotspots was not changed significantly (Fig 2D, black points). The reduction in the number and activity of hotspots was not due to depletion of leptotene/zygotene spermatocytes in CKO testes; in fact, the proportion of zygotene spermatocytes in CKO testes was slightly increased (Fig S1D).

PRDM9-dependent H3K36 trimethylation at hotspots (Powers et al. 2016; Altemose et al. 2017), was also reduced in CKO spermatocytes (Fig 2E. $p < 2\times10^{-16}$, Wilcoxon rank sum test). The reduction of hotspots in intergenic regions (Fig 2E, red dots) was stronger than those in actively transcribed genes (Fig 2E, grey dots. $p < 2\times10^{-16}$, Wilcoxon rank sum test) due to additional presence of H3K36me3 background associated with transcription. The reductions of H3K4me3 and H3K36me3 correlated with each other (Fig 2F).

Together, these results indicate that EWSR1 affects PRDM9-dependent H3K4 and H3K36 trimethylation in spermatocytes.

EWSR1 does not affect PRDM9 binding to hotspot DNA or PRDM9 multimerization *in vitro*

The mean H3K4me3 level at all PRDM9-dependent sites was much lower in CKO spermatocytes (Fig 2G, blue line) than in controls (Fig 2G, red line) and *Prdm9* heterozygous (*Prdm9*$^{+/-}$) spermatocytes (Baker et al. 2015b) (Fig 2G, yellow line).

Two possible explanations of the reduced H3K4me3 level at hotspots could be that EWSR1 affects PRDM9 binding to hotspot DNA or its multimerization (Baker et al. 2015b; Patel et al. 2016; Altemose et al. 2017). We tested the effect of EWSR1 on PRDM9 binding to hotspot DNA by electrophoretic mobility shift assay (EMSA) using two hotspot DNA fragments (Pbx1 (Billings et al. 2013) and Chr16-66.9Mb) and *E.coli* expressed and purified EWSR1 and PRDM9 (Fig S4B). In both experiments, the presence of EWSR1, which strongly binds PRDM9 *in vitro* (Parvanov et al. 2017), did not affect PRDM9 binding to hotspot DNA (Fig 2H and S4C). Next, we tested directly whether full-length PRDM9 molecules can form multimers *in vitro*, using PRDM9 fused to two different tags, 6HisHALO-MBP and MBP alone. The two fused proteins differ in their molecular weight (172 kDa and 127 kDa, respectively). PRDM9 molecules did bind to each other (Fig.S4D), and this interaction was not mediated by the MBP tag (Fig S4E). EWSR1 strongly interacted with PRDM9 (Fig 2I, lower panel, lane 6, and (Parvanov et al. 2017)), but did not affect the interaction between the PRDM9 molecules *in vitro* (Fig 2I, upper panel, lanes 4 and 6). These results show that PRDM9 can form multimer complexes independently, at least *in vitro*.

In summary, loss of EWSR1 affects the efficiency of H3K4/K36 trimethylation at meiotic hotspots *in vivo*, markedly decreasing their number and activity, but this effect does not seem to be due to changes in the strength of PRDM9 binding to hotspots or in its multimer formation, as judged by *in vitro* experiments.

Loss of EWSR1 affects DSB repair

To test whether EWSR1 also influences the subsequent steps of the recombination processes, we next determined the numbers, positions, and activities of DSBs in CKO and controls. The protein DMC1 marks the single stranded DNA tails at DSBs (Cohen et al. 2006). Counting the DMC1 foci number per cell, we observed no significant difference between CKO and controls in early leptotene and zygotene spermatocytes (Fig 3A).This result shows that the number of DSBs per meiosis is not dependent on the presence or absence of EWSR1.

To determine whether the locations or repair of DSB sites in CKO are affected, we performed ChIP-seq for DMC1 (Smagulova et al. 2011; Brick et al. 2012) (Fig S5A). First, we asked whether DSBs still occur at PRDM9-dependent sites in the absence of EWSR1 by DMC1 ChIP-seq. We detected 13,003 DMC1 peaks in CKO spermatocytes, 90.1% of which (11,715 peaks) overlapped with hotspots in controls (Fig 3B). 94.6% of shared DMC1 peaks (11,085 peaks) contain a PRDM9 binding site at their centers, and 78.0% of those (9,132 peaks) were also found by ChIP-seq for H3K4me3, indicating that a great majority of DSBs in CKO spermatocytes are indeed initiated at PRDM9 binding sites. The aggregation plots also confirmed that DSBs contain PRDM9 binding motifs at their centers in both control and CKO spermatocytes (Fig 3C).

Second, we asked whether the lack of EWSR1 affects DSB repair. In both CKO and controls, DSBs on the X chromosome showed higher activity compared to the autosomes (Fig S5B), reflecting the delay of the DSB repair on the X chromosome until mid-pachytene (Inagaki et al. 2010). On autosomes, the normalized overall activity of

DMC1 in CKO spermatocytes was increased compared to controls (p = 9.6 X 10^{-23}, Wilcoxon rank sum test), with a concomitant reduction on the X chromosome (p = 1.1 X 10^{-41}, Wilcoxon rank sum test, Fig 3D). This suggests that DSB repair on autosomes in the CKO is also delayed, which can explain the increased asynapsis we observed (Fig 1F).

Together, these data suggest that in the absence of EWSR1 DSBs are still formed at PRDM9-dependent hotspots, but their repair is delayed.

DSB formation at hotspots requires PRDM9-dependent histone methylation

Since there was a marked difference between the numbers of hotspot H3K4me3 and DMC1 peaks in CKO spermatocytes (7,858 hotspot H3K4me3 peaks, compared to 13,003 DMC1 peaks), we compared their positions and activities. We found that 38% of detected DMC1 peaks (3,478 peaks) do not show statistically significant H3K4 trimethylation in CKO spermatocytes. Since most of these sites (3,321 sites) have lower H3K4me3 levels in wild type controls, we asked whether DSBs initiated at PRDM9 binding sites that appear not to have acquired a H3K4me3 mark are truly occurring at sites lacking any H3K4me3, or are they occurring at sites whose H3K4me3 levels fall below the threshold of detection by the MACS peak calling algorithm. To distinguish unequivocally between these possibilities, we created a new *Prdm9*$^{Set-/Set-}$ mutant mouse model that retains its DNA binding specificity, but lacks any methyltransferase activity. In this model, a G274A amino acid substitution in PRDM9 causes a total loss of its methyltransferase activity, whereas a mutation at the PR/SET domain does not affect its DNA binding function (Diagouraga et al. 2018). Like other *Prdm9* mutants (Hayashi

et al. 2005; Sun et al. 2015; Imai et al. 2017; Parvanov et al. 2017; Diagouraga et al. 2018), *Prdm9*$^{Set-/Set-}$ homozygous mice are sterile, lacking any post-meiotic spermatids (Fig 3E, upper panels) and show a cytological phenotype consistent with pachytene stage-like arrest (Fig 3E, lower panels). PRDM9 protein level is reduced in the *Prdm9*$^{Set-/Set-}$ testes compared to wild type (Fig S5C), but its localization remains the same (Fig S5D). Hotspot H3K4 trimethylation in *Prdm9*$^{Set-/Set-}$ spermatocytes was completely absent (Fig 3F upper panel, purple line and S5E). DSBs in this mutant occurred at PRDM9-independent H3K4me3 sites (5,562 out of 5,698 detected peaks, or 97.6%), most of which were promoters or enhancers (Fig 3F lower panel and S5F, S5G).

We conclude that DSB formation at hotspots requires PRDM9-dependent H3K4 trimethylation of the nearby nucleosomes, and that DSBs in CKO spermatocytes occur at PRDM9-trimethylated H3K4 sites including those whose methylation levels are too low to be detected computationally. Our results conform with those obtained in a different SET mutant (Diagouraga et al. 2018).

DSB activity and distribution are altered in the absence of EWSR1

In wild type spermatocytes, DMC1 levels generally correlate with H3K4me3 level ($r = 0.59$, $p < 2.2 \times 10^{-16}$, Fig 4A). However, in CKO spermatocytes, many “undetectable” H3K4me3 hotspots at FDR > 0.01 (Fig 4B blue dots) show similar DMC1 level as H3K4me3 detectable hotspots (Fig 4B yellow dots), causing weaker correlation between H3K4me3 and DMC1 levels in CKO spermatocytes ($r = 0.30$, $p < 2.2 \times 10^{-16}$, Fig 4B).To investigate whether this results from reduced PRDM9 methyltransferase activity observed in CKO, we carried out DMC1 ChIP-seq in *Prdm9*$^{+/-}$ spermatocytes which

show similar reduction of H3K4me3 levels at hotspots (Fig 2G and (Baker et al. 2015b)). We detected 9,548 DMC1 peaks, of which only 76.8% (7,337 peaks) overlapped DMC1 sites in controls (Fig 4C and S6A), a significant difference compared to 90.1% overlap in CKO (Fig 3B). From the remaining 2,211 peaks, 1,606 (16.8% of the total) did not contain PRMD9 binding motif at the center. However, the correlation between DMC1 and H3K4me3 level in *Prdm9*$^{+/-}$ spermatocytes was similarly strong as in the controls ($r = 0.59$, $p < 2.2 \times 10^{-16}$; Fig 4D). This discrepancy led us to test whether the redistribution of DSB in the absence of EWSR1 is related to chromatin state (Walker et al. 2015). In B6 or *Prdm9*$^{+/-}$ spermatocytes, DMC1 levels were similar in open and closed chromatin ($p = 0.21$ in B6, $p = 0.10$ in *Prdm9*$^{+/-}$, Wilcoxon rank sum test, Fig 4E and 4F). In contrast, DSB activity was shifted towards closed chromatin in CKO spermatocytes ($p = 1.21 \times 10^{-12}$, Wilcoxon rank sum test; Fig 4G and S6B). In addition, this shift leads to the redistribution of DSBs along each chromosome (Fig S7). In most chromosomes, the shift of DSB activity towards closed chromatin can be seen on local level (Fig S7).

These results indicate that the reduced PRDM9 methyltransferase activity alone cannot explain the altered hotspot choice observed in *Ewsr1* CKO. They also suggest that one consequence of EWSR1 function in early meiotic prophase is affecting the selection of activated hotspots for DSB formation.

Lack of *Ewsr1* affects the number and distribution of genetic crossovers in meiosis

We tested whether the redistribution of DSBs caused by the loss of EWSR1 also affects the subsequent recombination events by determining the number and distribution of MLH1 foci, which mark virtually all crossover sites (Anderson et al. 1999) (Fig 5A). Crossover number was significantly lower in CKO spermatocytes (18.3 ± 2.6) compared to control spermatocytes (22.9 ± 1.4; p <0.001) (Fig 5B). This is less than the one crossover per chromosome required for normal meiosis. Indeed, at pachynema, about 70% of CKO spermatocytes lacked a crossover on the XY bivalent (yellow arrow in Fig 5B, right panel, and Fig S8A), and more than half had no crossover on at least one autosome (white arrow in Fig 5A, right panel, and Fig S8B).

In human and mouse, synaptonemal complex (SC) length is correlated with crossover number (Lynn et al. 2002; Petkov et al. 2007; Gruhn et al. 2013; Baier et al. 2014; Wang et al. 2017). Indeed, we observed a shorter SC length at pachynema in CKO spermatocytes (158.4 ± 20.4 µm) compared with *Ewsr1* control spermatocytes (184.7 ± 20.0 µm) (Fig 5C).

The reduction of the total number of crossovers could be due to change in interference distance, because genetic interference is dependent on SC length (Petkov et al. 2007), but this proved not to be the case. Instead, the reduction in the number of MLH1 foci was related to crossover repositioning along the chromosomes. The decrease of MLH1 foci numbers in *Ewsr1* CKO compared to control spermatocytes occurred similarly in long and middle-sized autosomes as evidenced by chromosomes 1 and 11 (Fig S8C and S8D). In both chromosomes, we scored lower number of bivalents with more than one MLH1 focus. However, this reduction was not caused by longer interference distance in the mutant (Fig S8E) measured by the average SC distance

between two foci on the same bivalent (de Boer et al. 2006). MLH1-positive cells with double crossovers on chromosome 1 or 11 showed identical crossover distribution patterns in CKO and control spermatocytes (Fig S8F top panels). In CKO, the crossovers were more evenly distributed along the chromosomes compared to control spermatocytes in which crossovers are preferentially formed near the telomeres with a second frequency peak in the centromere-proximal third of the bivalents (Fig 5D and S7F bottom panels). This redistribution in CKO increases the likelihood of single crossovers and decreases the likelihood of two or more crossovers per bivalent.

These results suggest that the absence of EWSR1 in early meiotic prophase affects downstream steps in the recombination pathway, including the choice of which H3K4me3-marked recombination hotspots will undergo DSBs and will ultimately be resolved as crossovers.

EWSR1 links PRDM9-activated hotspots with the chromosome axis elements through pREC8-containing cohesin complexes

How does EWSR1 affect PRDM9 function and regulate DSB formation and crossover pathway? Based on our previous finding showing that EWSR1 binds strongly to pREC8 (Parvanov et al. 2017), we used co-immunoprecipitation (co-IP) to test whether EWSR1 mediates the connection between PRDM9, hotspot DNA, and chromosome axis cohesins. We detected a strong co-IP signal between EWSR1 and the meiosis specific kleisin cohesin subunit pREC8 (Fig 6A). This interaction was retained after DNase I treatment, indicating direct interaction between EWSR1 and pREC8. The other meiosis specific kleisin subunit, RAD21L, showed very weak signal

in EWSR1 co-IP, which became almost undetectable after DNase I treatment, indicating these interactions were indirect, caused by both proteins binding to DNA. The SC proteins SYCP3 and SYCP1 (Fig S9 and (Parvanov et al. 2017)) did not show any interaction with EWSR1. In *Prdm9*$^{-/-}$ spermatocytes, the interaction between EWSR1 and pREC8 is preserved. This interaction is also retained in the *Prdm9*$^{tm3.1Kpgn}$ mutant mice, which express a PRDM9 fragment lacking its zinc finger domain that is unable to bind DNA or trimethylate histone 3 at hotspots (hereafter *Prdm9*$^{\Delta ZnF/\Delta ZnF}$) (Parvanov et al. 2017). However, this mutant PRDM9 shows no interaction with pREC8, and has dramatically reduced interaction with EWSR1 even though its EWSR1-binding N-terminal domain is preserved (Parvanov et al. 2017). These observations suggest that the association between EWSR1, PRDM9 and pREC8 might require either retaining the DNA binding and/or methyltransferase activity of PRDM9.

To distinguish between these possibilities, we performed co-IPs with EWSR1 in spermatocytes of *Prdm9*$^{\Delta ZnF/\Delta ZnF}$ and *Prdm9*$^{Set-/Set-}$ mice. Similar to wild type PRDM9, EWSR1 showed a strong interaction with pREC8 in these mutants (Fig 6B), but did not co-IP PRDM9 in either mutant (Fig 6B, left and middle panels, and (Parvanov et al. 2017)). However, co-IP with PRDM9 did detect interactions with EWSR1 and REC8 in *Prdm9*$^{Set-/Set-}$ spermatocytes (Fig 6B, right panel), so the negative result in the reverse direction was most likely due to the lower PRDM9 protein amount in this mutant (Fig S5C). These results suggest that the interaction between EWSR1 and pREC8 is independent of the presence or effective function of PRDM9. Loss of PRDM9's DNA binding activity but not methyltransferase activity disrupts the interaction between

PRDM9 and EWSR1, resulting in disassociation between PRDM9 and the cohesin complexes.

To confirm that EWSR1 is essential for the association between PRDM9 and pREC8, we performed co-IP with PRDM9 in the CKO and control testes. In the controls, PRDM9 binds to both EWSR1 and pREC8 with or without DNase I treatment (Fig 6C, left four lanes). In CKO spermatocytes, PRDM9 shows some interaction with pREC8 without DNase I treatment, which is dramatically reduced after DNase I treatment (Fig 6C, lower panel, right four lanes). As expected, PRDM9 does not interact with EWSR1 in the mutant after DNAse I treatment (Fig 6C, upper panel, lane 8) because the two proteins are not expressed together in germ cells; the apparent interaction without DNAse I ((Fig 6C, upper panel, lane 7) most probably stems from EWSR1 from somatic cells associating with DNA after cell lysis, or incomplete EWSR1 excision in the small portion of spermatocytes (Fig S1A).

These data indicate that EWSR1 indeed mediates the association between PRDM9 and the chromosome axis elements via binding to pREC8.

Discussion

EWSR1 appears to be an important protein in early meiotic prophase whose action influences all subsequent recombination events, including the imposition of PRDM9-dependent H3K4/K36 trimethylation marks activating recombination hotspots, their subsequent usage for DSB formation, and the choice of DSBs destined for the crossover formation. It does so by affecting two major processes. The first affected process is PRDM9-dependent H3K4/K36 trimethylation. The second process is

PRDM9-hotspot complex association with the nascent chromosome axis through pREC8. Although EWSR1 participates in hotspot association with the chromosome axis, out data suggests that it cannot be the only protein to do so, because a significant share of PRDM9-dependent hotspots are forming DSB in the CKO. Another prominent candidate, CXXC1, does not seem to be important in the PRDM9-dependent hotspot recognition pathway (Tian et al. 2018), which raises the question about what other proteins may be involved in this process, if any. In consideration of other possible functions of EWSR1 in early meiosis suggested by its functions in somatic cells, we did not find any RNA-related function of EWSR1 despite our considerable efforts to match the findings reported there (Fisher 2014; Schwartz et al. 2015).

EWSR1 enhances PRDM9 methyltransferase activity *in vivo*

In humans and mice, PRDM9 is the only known protein that determines the positions of meiotic hotspots (Baudat et al. 2010; Myers et al. 2010; Parvanov et al. 2010) through its binding to specific DNA sequences and trimethylation of H3K4 and H3K36 at the adjacent nucleosomes (Smagulova et al. 2011; Baker et al. 2014; Powers et al. 2016). Loss of PRDM9 (Hayashi et al. 2005; Brick et al. 2012; Sun et al. 2015; Parvanov et al. 2017) or any of its functional domains – zinc fingers for DNA binding (Parvanov et al. 2017), PR/SET for methyltransferase activity (Fig 3 and S4), or KRAB domain for protein interactions (Imai et al. 2017) result in germ cell apoptosis due to meiotic arrest. Here we found that EWSR1 influences the methyltransferase activity of PRDM9. Lack of EWSR1 causes two- to four-fold reduction of both H3K4 and H3K36 methyltransferase activities at all PRDM9 activity levels (Fig 2D, 2E). This observation is

not likely to be due to H3K4/36 methyltransferase activity of EWSR1, because it has no histone modification related domain (Schwartz et al. 2015). EWSR1 could serve as activator of the PR/SET domain; however, this is unlikely, because purified full-length PRDM9 is fully capable of performing its two methyltransferase activities *in vitro* (Powers et al. 2016).

One plausible explanation is that loss of EWSR1 may affect PRDM9 methyltransferase activity by shifting the balance of PRDM9 binding to other proteins in the process of its interaction with hotspot DNA and/or with adjacent nucleosomes during meiotic initiation. We and others have identified several PRDM9 interaction proteins besides EWSR1, which involve histone modification readers or writers, such as H3K4me3 recognition protein CXXC1 (Imai et al. 2017; Parvanov et al. 2017), histone acetyl reader CDYL, H3K9 methyltransferase EHMT2 (Parvanov et al. 2017). These proteins interact with PRDM9 through its KRAB and adjacent domains (Parvanov et al. 2017). CXXC1 is known to inhibit or restrict the activity of the Setd1A histone H3K4 methyltransferase complex (Tate et al. 2010). Its binding to PRDM9 could possibly have a similar effect on PRDM9 methyltransferase activity in the absence of EWSR1. Alternatively, CDYL and EHMT2, which bind to PRDM9 through a region overlapping the SET domain, may act as inhibitors of PRDM9 H3K4 methyltransferase activity. In somatic tissues, these two proteins form a complex that can methylate H3K9 and serve as a transcription repressor by imposing a closed chromatin mark (Mulligan et al. 2008). Their expression pattern in spermatocytes suggests that they may be replaced as PRDM9 partners by EWSR1 and/or CXXC1 (Parvanov et al. 2017).Therefore, EWSR1

binding to PRDM9 may be necessary to release the activity of its SET domain *in vivo*. These possibilities are not mutually exclusive.

EWSR1 interacts with meiosis specific cohesin pREC8 during meiosis

During meiosis, EWSR1 interacts not only with PRDM9 but also with the phosphorylated form of the meiosis specific cohesin REC8. This interaction is independent of the presence or absence of PRDM9 (Fig 6 and (Parvanov et al. 2017)). Conversely, PRDM9 association with pREC8 and synaptonemal complex proteins is dependent on its binding to hotspot DNA (Parvanov et al. 2017). Here we show that EWSR1 is necessary for PRDM9-hotspot DNA association with the cohesin elements of the chromosome axis, providing direct link to pREC8. EWSR1 does not seem to interact with the other meiosis specific kleisin cohesin subunit, RAD21L (Fig 6A and 6B). Loss of PRDM9's DNA binding, but not its methyltransferase activity, abolishes the association between PRDM9 and EWSR1 in spermatocytes (Fig 6B and (Parvanov et al. 2017)), which suggests that PRDM9 binding to DNA is necessary for stabilization of the PRDM9-EWSR1 complex.

Our results suggest the possibility that the two EWSR1 functions in meiosis – enhancing PRDM9-dependent H3K4/K36 trimethylation and providing a link between PRDM9 and pREC8 – may not be independent from each other. It is plausible that linking PRDM9-bound hotspots to the chromosome axis might stabilize the entire complex and allow effective H3K4/K36 trimethylation.

In yeast, Rec8 is required for normal DSB distribution and repair (Kugou et al. 2009; Kohler et al. 2017). In mice, loss of REC8 causes meiotic arrest, asynapsis and DSBs

formation defects (Bannister et al. 2004; Xu et al. 2005; Ward et al. 2016). Moreover, in yeast and mammals, pREC8 is required for REC8 cleavage and meiotic prophase I progress (Buonomo et al. 2000; Eijpe et al. 2003; Lee et al. 2003; Brar et al. 2006), and is essential for crossover determination and synaptonemal complex formation (Yoon et al. 2016). Consequently, the EWSR1-dependent association between PRDM9-activated hotspots and pREC8 may promote proper DSB formation and crossover pathway choice, which can explain the altered DSB distribution, increased chromosomal asynapsis, and changes in crossover number and distribution in *Ewsr1* CKO spermatocytes.

The complex between EWSR1-PRDM9 affects the fate of subsequent recombination events

In *Ewsr1* CKO spermatocytes, although the hotspot H3K4me3 number and level are remarkably reduced and the association between PRDM9 and chromosome axis elements is impaired, the number of DSB per cell is not significantly changed (Fig 3A). This conforms with the presence of a homeostatic mechanism regulating the numbers of recombination events at several levels (Cole et al. 2012) and our previous observation that the number of DSB is independent on *Prdm9* dose or hotspot trimethylation level (Sun et al. 2015). Importantly, DSBs do not occur at PRDM9 binding sites in *Prdm9*$^{Set-/Set-}$ mice, confirming that PRDM9 binding is not sufficient to initiate DSBs at hotspots but also requires its H3K4/K36 trimethylation activity (see also (Diagouraga et al. 2018)). In the absence of EWSR1, the positions of DSBs are not significantly correlated with the H3K4me3 levels. This suggests that EWSR1 is actively

involved in associating hotspots with specific cohesin complexes forming the chromosome axis and promoting recombination (Ishiguro et al. 2011), although possibly not the only protein to do so. In absence of EWSR1, CXXC1 could link PRDM9-trimethylated hotspots to another chromosome axis element, IHO1, which is not a cohesin (Imai et al. 2017). This alternative pathway can explain the shift of DSB activity along the chromosomes and towards closed chromatin (Fig 4G) in the CKO, which could reflect either a true increase in DSB frequency in closed chromatin, or, more likely, that DSBs are equally initiated in open and closed chromatin but those in closed chromatin need longer time to repair.

The shifted pattern of DSB initiation towards closed chromatin and away from telomeres affects the subsequent recombination repair pathways and results in reduced number of crossovers to less than one crossover per bivalent, thereby breaking the crossover assurance efficiency (Kneitz et al. 2000; Berchowitz and Copenhaver 2010; Reynolds et al. 2013; Holloway et al. 2014). This reduced number is not a result from increase in crossover interference; it reflects the more random crossover positioning in CKO losing the typical wild type pattern of bimodal distribution of crossovers relative to the centromere-telomere axis (Paigen et al. 2008; Billings et al. 2010; Liu et al. 2014). As a result, both the fraction of bivalents with double or triple crossovers and the SC length are reduced (Fig 5); the latter is known to correlate strongly with DSB and crossover number (Carofiglio et al. 2013; Baier et al. 2014).

The reduced SC length in *Ewsr1* CKO is reminiscent of that of *Rec8* mutant (Agostinho et al. 2016; Ward et al. 2016), further suggesting that the two proteins act in the same recombination pathway. In the *Ewsr1* CKO spermatocytes, reduction of SC

length and crossover number is similar, which indicates that loss of EWSR1 alters DSB repair pathways most likely through disassociation between hotspots and pREC8.

Model of EWSR1 action at the early stages of recombination activation pathway

Our results suggest the following model of EWSR1 action in early meiotic prophase. In leptonema, a recombination-initiating complex of PRDM9 dimer/oligomer – hotspot DNA forms (Fig.7, top panel). EWSR1 joins the complex and simultaneously binds to pREC8, incorporating the recombination initiation complex into the nascent chromosome axis and resulting in more efficient H3K4/K36 trimethylation at the nearby nucleosomes (Fig 7, bottom left panel, up). The preferential link to meiotic-specific cohesin complexes containing pREC8 promotes the crossover pathway of DSB repair (Martini et al. 2011; Tang et al. 2015) and ensures correct positioning of crossovers relative to the centromere-telomere axis (Fig 7, bottom left panel, down).

When PRDM9 methyltransferase activity is impaired, EWSR1 still links the recombination initiation complex with REC8-containing cohesin axis, but DSBs cannot be initiated at PRDM9-binding sites and occur at other H3K4me3 sites instead (Fig 7, bottom right panel). In the absence of EWSR1, PRDM9-dependent trimethylation of H3K4/K36 is inefficient (Fig 7, bottom central panel, up). The recombination initiation complexes are not actively associated with pREC8. DSBs are formed at PRDM9-trimethylated sites through an alternative pathway that might or might not involve cohesins (Fig.7, bottom central panel, down). In turn, this results in shifted positioning of crossovers relative to the centromere-telomere axis and disruption of crossover

assurance, leaving some bivalents without crossovers and causing germ cell apoptosis in late prophase I.

Material and Methods

Histology

Testis or epididymis from adult B6, *Prdm9*$^{Set-/Set-}$, *Ewsr1* control or CKO mice were dissected out, fixed with Bouin's solution, and embedded in paraffin wax, and 5-μm sections were prepared. Sections of testis were stained with Periodic acid–Schiff–diastase (PAS), and section of epididymis were stained with hematoxylin and eosin (HE) using standard techniques.

TUNEL assay

For detection of apoptosis in tissues, testis sections from *Ewsr1* control (n = 3) and CKO (n = 3) were subjected to fluorescence labeling of DSBs by terminal deoxynucleotidyl transferase–mediated digoxigenin-dUTP nick-end labeling (TUNEL) assay, using the In Situ Cell Death Detection Kit (Roche, 11684795910) according to the manufacturer's protocol.

Chromosome spreads

The drying-down technique (Peters et al. 1997) was used for preparation of chromosome spreads from spermatocytes. The slides were immunolabeled with anti-PRDM9 (1:200, custom-made), SYCP3 (1:400, Novus, NB300-231), γH2AX (1:1000, Abcam, ab26350), BRCA1 (1:200, Santa Cruz, sc-642), ATR (1:500, Santa Cruz, sc-1887), HORMAD1 (1:500, Protein Tech, 13917-1-AP), H3K4me3 (1:1000, Millipore, 07-

473), H1t (1:1000, gift from Mary Ann Handel), DMC1 (1:200, Santa Cruz, sc-8973) or MLH1 (1:100, BD Pharmingen, 550838) antibodies.

H3K4me3 and H3k36me3 ChIP-seq and analysis

H3K4me3 and H3k36me3 ChIP was performed in two replicates with 14 dpp B6 and *Ewsr1* CKO spermatocytes, and one replicate with 14 dpp *Prdm9*$^{Set-/Set-}$ spermatocytes, using the protocol we reported previously (Baker et al. 2014). ChIP libraries were sequenced on an Illumina® HiSeq 2500 platform, with 75 bp single-end reads. The reads were trimmed for quality using trimmomatic (v.0.32), and then aligned to the mouse mm10 genome using BWA (v.0.5.10-tpx). Data are available at NCBI Gene Expression Omnibus (GEO; http://www.ncbi.nlm.nih.gov/geo) under accession number GSE108259 (Accession for review purpose: https://www.ncbi.nlm.nih.gov/geo/query/acc.cgi?acc=GSE108259). H3K4me3 or H3K36me3 activity was normalized to reads per million (rpm). Peak calling was performed using MACS (v.1.4.2) with standard treatment (ChIP) and control (input) samples with a false discovery rate (FDR) value 0.01. *Prdm9*^{Dom2} hotspot locations were previously described by (Walker et al. 2015) (GSE52628) and lifted over to the mouse genome version mm10. Open or closed chromatin regions in spermatocytes were determined by H3K9me3 domains, which were previously described by (Walker et al. 2015) (GSE61613) and also lifted over to the mouse mm10 genome. H3K4me3 peaks shared by B6, *Prdm9*$^{Set-/ Set-}$ and CKO spermatocytes, inside and outside known hotspots, in open/closed chromatin regions or H3K36me3 peaks in genic/intergenic regions were determined using bedtools (v2.22.0) intersect. Wilcoxon rank sum test was used to calculate the statistical significance. Analyses for the aggregation plots were

carried out using the Aggregation and Correlation Toolbox (ACT) (Jee et al. 2011). ACT parameters were: nbins = 500, mbins = 0, radius = 1500.

DMC1 ChIP-seq

DMC1 ChIP was performed with two replicates of 8 weeks old B6,*Prdm9*$^{Set-/Set-}$, *Prdm9*$^{+/-}$and *Ewsr1* CKO spermatocytes using an established method (Khil et al. 2012). Briefly, after cross-linking the testes with 1% paraformaldehyde solution for 10 min, the tissue was homogenized and the nuclei were isolated. The chromatin was then sheared to ~1000 bp by sonication. 2 µl of chromatin was saved as input. The rest of chromatin was incubated with antibody against DMC1 overnight at 4°C, and then with protein G Dynabeads (Thermo Fisher Scientific, 10004D) for 4 hrs at 4°C. The beads were washed with Wash buffer 1 (0.1% SDS, 1% Triton X-100, 2 mM EDTA, 20 mM Tris-HCl, pH 8.0, 150 mM NaCl), Wash buffer 2 (0.1% SDS, 1% Triton X-100, 2mM EDTA, 20mMTris-HCl, pH 8.0, 500 mM NaCl), Wash buffer 3 (0.25 M LiCl, 1% NP-40, 1mM EDTA, 10mMTris-HCl, pH 8.0, 1% Deoxycholic acid) and twice with TE buffer. The chromatin was eluted with dilution buffer (1% SDS, 0.1 M $NaHCO_3$ pH 9.0) at 65°C for 30 min and reverse-crosslinked by adding 200 mM NaCl and incubation overnight at 65°C. The libraries were then prepared by established method (Khil et al. 2012), sequenced on an Illumina® HiSeq 2500 platform, with 75 bp paired-end reads..

Co-immunoprecipitation assays

The co-IP was carried out using our reported protocol (Parvanov et al. 2017). Briefly, For the DNase I-treated co-IP samples, testes extract of twenty 14 dpp B6, *Prdm9*$^{\Delta ZnF/\Delta ZnF}$, *Prdm9*$^{Set-/Set-}$, *Ewsr1* control or CKO mice was added with 100 µl of DNase I buffer and 20 U DNase I (ThermoFisher Scientific, AM1906), and incubated for

1 hr at room temperature. After incubation, 10% of extract was set apart as input. The co-IP was perform by incubating extract with protein A or G Dynabeads conjugated with antibodies against PRDM9 or EWSR1 (sc-6532, Santa Cruz) overnight at 4°C. IgG from the same animal species was used as negative control. The samples were eluted with GST buffer (0.2 M glycine, 0.1% SDS, 1% Tween 20, pH 2.2) and neutralized 1 M Tris-HCl, pH 8. After heated at 95°C for 5 min, 10 µg of IP and input samples were then subjected to electrophoresis and western blotting for detection of PRDM9 (1:1000), EWSR1 (1:1000, Abcam, ab54708), REC8 (1:1000, Abcam, ab38372), RAD21L (1:600, gift from Jibak Lee), SYCP3 (1:1000) or SYCP1 (1:1000).

Acknowledgments

We thank Anita Adams and Catrina Spruce for technical help, Mary Ann Handel and Jibak Lee for sharing their antibodies, and Ken Paigen and Ruth L. Saxl for critical reading and helpful suggestions. This work was supported by National Institutes of Health Grants R01 GM078452 to P.M.P., P50 GM076468 to GaryChurchill/Project B to P.M.P., and Cancer Core Grant CA34196 to the Jackson Laboratory.

Author contributions

HT and PMP* designed the experiments. HT, TB, PMP and CLB performed the experiments. HT, MW and PMP* analyzed the results. HT and PMP* wrote the paper.

Figure Legends

Fig 1. *Ewsr1* CKO mice are sterile with meiotic arrest and chromosomal asynapsis in spermatocytes.

(A) Fertility test in *Ewsr1* control (n = 4) and CKO (n = 3) male mice. (B) Testis index (testis weight/body weight) in *Ewsr1* control and CKO mice. (C) Top panels - PAS staining of seminiferous tubule sections. Bottom panels - H&E staining of epididymis sections. Left panels - control; right panels - *Ewsr1* CKO (right). Scale bar, 50 µm. (D and E) Apoptosis in the *Ewsr1* CKO and control testes. (D) TUNEL staining in *Ewsr1* control and CKO testis. Scale bar, 50 µm. (E) Apoptotic cell number is quantized as TUNEL positive cell number per tubule cross section in *Ewsr1* control and CKO. (F) Spermatocyte chromosome spreads of control and CKO stained for γH2AX (magenta) and SYCP3 (green). Arrow in middle panel shows XY chromosomes asynapsis. Arrow in right panel shows autosome and XY asynapsis. Scale bar, 10 µm. Bars in (A), (B) and (E) represent mean ± SD. ** $p < 0.01$, *** $p < 0.001$, by Student's *t*-test.

Fig 2. H3K4me3 and H3K36me3 activities at hotspots are reduced in *Ewsr1* CKO.

(A) Chromosome spreads on *Ewsr1* control and CKO stained for PRDM9 (green), H3K4me3 (green) and SYCP3 (red). Scale bar, 10 µm. (B) Venn diagram of H3K4me3 ChIP-seq hotspot peaks in control (pink) and CKO (blue) spermatocytes. (C) Distribution of H3K4me3 hotspot frequency levels in B6 control (white) and *Ewsr1* CKO (grey). (D) MA-plot of shared H3K4me3 peaks in B6 and *Ewsr1* CKO mice. Red dots, PRDM9-defined H3K4me3 hotspots, n = 6,679; black dots, H3K4me3 peaks at non-hotspots, n = 54,434. (E) MA-plot of H3K36me3 reads in PRDM9-defined H3K4me3 hotspots from *Ewsr1* CKO and control spermatocytes. Red dots, hotspot in intergenic

region, n = 6,082. Black dots, hotspot in genic region, n = 4,791. (F) Correlation between H3K4me3 and H3K36me3 level at hotspots in B6 control (red dots) and CKO mice (blue dots). (G) Aggregation plots of H3K4me3 signal in B6 (red lines), *Prdm9*$^{+/-}$ (yellow lines) and *Ewsr1* CKO (blue lines) spermatocytes, centered at the PRDM9 binding site. Left, mean rpm counts. (H) EMSA with MBP-PRDM9 and Pbx1 hotspot in the presence or absence of 6His-HALO-EWSR1. Red arrow, shifted band; black arrow, unbound fragment. Right, quantification of shifted fraction. Data represent mean ± SD. *** $p < 0.001$, N.S., not significant, by two-way ANOVA. (I) Pull-down assay with purified 6HisHALO-MBP-PRDM9, MBP-PRDM9 and GST-EWSR1. SN, supernatant. Beads, elution from beads.

Fig 3. EWSR1 does not affect the total number of DSBs per cell.

(A) Left - DMC1 staining on *Ewsr1* control and CKO chromosome spread. Scale bar, 10 µm. Right – distribution plot of DMC1 foci in leptotene and zygotene spermatocytes. Bars represent mean ± SD. $p = 0.96$ by Student's *t*-test. (B) DMC1 peaks occur at the same sites in B6 control (pink) and CKO (blue) spermatocytes. (C) Aggregation plot of H3K4me3 and DMC1 signal in B6 control (left) and CKO (right). The signal was normalized to the maximum signal. (D) MA-plot of activity of DSBs on autosomes (black dots, n = 8,744) and X chromosome (red dots, n = 388) from *Ewsr1* CKO and control spermatocytes. (E) PAS staining (upper panels) and SYCP3/γH2AX (lower panels) staining B6 and *Prdm9*$^{Set-/Set-}$ seminiferous tubule cross sections. Scale bar, 100 µm in upper panels, 20 µm in lower panels. (F) Aggregation plots of H3K4me3 (upper panel)

and DMC1 (lower panel) signal in B6 (red lines) and *Prdm9*$^{Set-/Set-}$ (purple lines) spermatocytes.

Fig 4. EWSR1 affects DSB distribution between open and closed chromatin.

(A and B) Correlation between DMC1 level and H3K4me3 level in B6 (A) and *Ewsr1* CKO (B). Yellow dots, hotspots with significant H3K4me3 peaks in both control and CKO (FDR < 0.01). Blue dots, hotspots with significant H3K4me3 peaks in controls but not significant in CKO (FDR > 0.01). (C) Dosage effect of PRDM9 on hotspot initiation. Venn diagram of the DMC1 peaks identified from DMC1 ChIP-seq in control (pink) and *Prdm9*$^{+/-}$ (yellow) spermatocytes. (D) Correlation between DMC1 level and H3K4me3 level in *Prdm9*$^{+/-}$. Yellow dots, hotspots with significant H3K4me3 peaks in both control and CKO (FDR < 0.01). Blue dots, hotspots with significant H3K4me3 peaks in controls but not significant in CKO (FDR > 0.01). (E, F and G) Frequency distribution of DMC1 activity in B6 (E), *Prdm9*$^{+/-}$ (F) and CKO (G) at hotspots in open (blue) and closed (red) chromatin.

Fig 5. Crossover number and length of SC are reduced in *Ewsr1* CKO.

(A) Presence of bivalents without crossovers in *Ewsr1* CKO. MLH1 (green) and SYCP3 (magenta) staining in *Ewsr1* control and CKO chromosome spread. White arrow, autosome with no crossover; yellow arrow, sex chromosomes with no crossover. Scale bar, 10 µm. (B) Distribution of the number of MLH1 foci in pachytene spermatocytes. (C) Distribution of the synaptonemal complex lengths. (D) Cumulative plots of crossovers on chromosome 1 (left) and chromosome 11 (right).

Bars in (C) and (D) are mean ± SD. ***$p < 0.001$ by Student's *t*-test.

Fig 6. EWSR1 interacts with meiotic cohesin protein pREC8.

(A) Co-IP with anti-EWSR1 in 14-dpp control testis extract stained for PRDM9 and cohesin proteins from 14 dpp B6 spermatocytes. In each blot, lane 1 – input; lane 2 – co-IP with non-immune IgG; lane 3 – co-IP with anti-EWSR1 untreated with DNAse I; lane 4 – co-IP with anti-EWSR1 treated with DNAse I. (B) Co-IP with anti-EWSR1 and anti-PRDM9 in 14 dpp *Prdm9*$^{\Delta ZnF/\Delta ZnF}$ and *Prdm9*$^{\Delta Set/\Delta Set}$ testis extract. In each blot, lane 1 – input; lane 2 – co-IP with non-immune IgG; lane 3 – co-IP with anti-EWSR1 untreated with DNAse I. (C) Co-IP with anti-PRDM9 in 14 dpp *Ewsr1* control (lanes 1-4) and CKO (lanes 5-8) testis extracts. In each blot, lanes 1 and 5 – input; lanes 2 and 6 – co-IP with non-immune IgG; lanes 3 and 7 – co-IP with anti-EWSR1 untreated with DNAse I; lanes 4 and 8 – co-IP with anti-EWSR1 treated with DNAse I.

Fig 7. Model of EWSR1 action in early meiosis.

EWSR1 is involved in hotspot activation and the association of hotspot DNA-PRDM9 and chromosome axis cohesins. See text for details.

References

Agostinho, A., O. Manneberg, R. van Schendel, A. Hernandez-Hernandez, A. Kouznetsova, H. Blom, H. Brismar, and C. Hoog. 2016. High density of REC8 constrains sister chromatid axes and prevents illegitimate synaptonemal complex formation. *EMBO Rep* **17**: 901-13.

Altemose, N., N. Noor, E. Bitoun, A. Tumian, M. Imbeault, J.R. Chapman, A.R. Aricescu, and S.R. Myers. 2017. A map of human PRDM9 binding provides evidence for novel behaviors of PRDM9 and other zinc-finger proteins in meiosis. *Elife* **6**.

Anderson, L.K., A. Reeves, L.M. Webb, and T. Ashley. 1999. Distribution of crossing over on mouse synaptonemal complexes using immunofluorescent localization of MLH1 protein. *Genetics* **151**: 1569-1579.

Baier, B., P. Hunt, K.W. Broman, and T. Hassold. 2014. Variation in Genome-Wide Levels of Meiotic Recombination Is Established at the Onset of Prophase in Mammalian Males. *Plos Genetics* **10**.

Baker, C.L., S. Kajita, M. Walker, R.L. Saxl, N. Raghupathy, K. Choi, P.M. Petkov, and K. Paigen. 2015a. PRDM9 drives evolutionary erosion of hotspots in Mus musculus through haplotype-specific initiation of meiotic recombination. *PLoS Genet* **11**: e1004916.

Baker, C.L., P. Petkova, M. Walker, P. Flachs, O. Mihola, Z. Trachtulec, P.M. Petkov, and K. Paigen. 2015b. Multimer Formation Explains Allelic Suppression of PRDM9 Recombination Hotspots. *PLoS Genet* **11**: e1005512.

Baker, C.L., M. Walker, S. Kajita, P.M. Petkov, and K. Paigen. 2014. PRDM9 binding organizes hotspot nucleosomes and limits Holliday junction migration. *Genome Res* **24**: 724-32.

Bannister, L.A., L.G. Reinholdt, R.J. Munroe, and J.C. Schimenti. 2004. Positional cloning and characterization of mouse mei8, a disrupted allelle of the meiotic cohesin Rec8. *Genesis* **40**: 184-94.

Baudat, F., J. Buard, C. Grey, A. Fledel-Alon, C. Ober, M. Przeworski, G. Coop, and B. de Massy. 2010. PRDM9 Is a Major Determinant of Meiotic Recombination Hotspots in Humans and Mice. *Science* **327**: 836-840.

Berchowitz, L.E. and G.P. Copenhaver. 2010. Genetic Interference: Don't Stand So Close to Me. *Current Genomics* **11**: 91-102.

Berg, I.L., R. Neumann, K.W. Lam, S. Sarbajna, L. Odenthal-Hesse, C.A. May, and A.J. Jeffreys. 2010. PRDM9 variation strongly influences recombination hot-spot activity and meiotic instability in humans. *Nat Genet* **42**: 859-63.

Billings, T., E.D. Parvanov, C.L. Baker, M. Walker, K. Paigen, and P.M. Petkov. 2013. DNA binding specificities of the long zinc-finger recombination protein PRDM9. *Genome Biol* **14**: R35.

Billings, T., E.E. Sargent, J.P. Szatkiewicz, N. Leahy, I.Y. Kwak, N. Bektassova, M. Walker, T. Hassold, J.H. Graber, K.W. Broman, and P.M. Petkov. 2010. Patterns of recombination activity on mouse chromosome 11 revealed by high resolution mapping. *PLoS One* **5**: e15340.

Borner, G.V., N. Kleckner, and N. Hunter. 2004. Crossover/noncrossover differentiation, synaptonemal complex formation, and regulatory surveillance at the leptotene/zygotene transition of meiosis. *Cell* **117**: 29-45.

Brar, G.A., B.M. Kiburz, Y. Zhang, J.E. Kim, F. White, and A. Amon. 2006. Rec8 phosphorylation and recombination promote the step-wise loss of cohesins in meiosis. *Nature* **441**: 532-6.

Brick, K., F. Smagulova, P. Khil, R.D. Camerini-Otero, and G.V. Petukhova. 2012. Genetic recombination is directed away from functional genomic elements in mice. *Nature* **485**: 642-645.

Buard, J., P. Barthes, C. Grey, and B. de Massy. 2009. Distinct histone modifications define initiation and repair of meiotic recombination in the mouse. *EMBO J* **28**: 2616-24.

Buonomo, S.B., R.K. Clyne, J. Fuchs, J. Loidl, F. Uhlmann, and K. Nasmyth. 2000. Disjunction of homologous chromosomes in meiosis I depends on proteolytic cleavage of the meiotic cohesin Rec8 by separin. *Cell* **103**: 387-98.

Carofiglio, F., A. Inagaki, S. de Vries, E. Wassenaar, S. Schoenmakers, C. Vermeulen, W.A. van Cappellen, E. Sleddens-Linkels, J.A. Grootegoed, H.P. Te Riele, B. de Massy, and W.M. Baarends. 2013. SPO11-independent DNA repair foci and their role in meiotic silencing. *PLoS Genet* **9**: e1003538.

Cobb, J., B. Cargile, and M.A. Handel. 1999. Acquisition of competence to condense metaphase I chromosomes during spermatogenesis. *Dev Biol* **205**: 49-64.

Cohen, P.E., S.E. Pollack, and J.W. Pollard. 2006. Genetic analysis of chromosome pairing, recombination, and cell cycle control during first meiotic prophase in mammals. *Endocr Rev* **27**: 398-426.

Cole, F., L. Kauppi, J. Lange, I. Roig, R. Wang, S. Keeney, and M. Jasin. 2012. Homeostatic control of recombination is implemented progressively in mouse meiosis. *Nat Cell Biol* **14**: 424-30.

de Boer, E., P. Stam, A.J. Dietrich, A. Pastink, and C. Heyting. 2006. Two levels of interference in mouse meiotic recombination. *Proc Natl Acad Sci U S A* **103**: 9607-12.

Diagouraga, B., J.A.J. Clement, L. Duret, J. Kadlec, B. de Massy, and F. Baudat. 2018. PRDM9 Methyltransferase Activity Is Essential for Meiotic DNA Double-Strand Break Formation at Its Binding Sites. *Mol Cell*.

Eijpe, M., H. Offenberg, R. Jessberger, E. Revenkova, and C. Heyting. 2003. Meiotic cohesin REC8 marks the axial elements of rat synaptonemal complexes before cohesins SMC1beta and SMC3. *J Cell Biol* **160**: 657-70.

Fisher, C. 2014. The diversity of soft tissue tumours with EWSR1 gene rearrangements: a review. *Histopathology* **64**: 134-50.

Gruhn, J.R., C. Rubio, K.W. Broman, P.A. Hunt, and T. Hassold. 2013. Cytological studies of human meiosis: sex-specific differences in recombination originate at, or prior to, establishment of double-strand breaks. *PLoS One* **8**: e85075.

Hassold, T. and P. Hunt. 2001. To err (meiotically) is human: the genesis of human aneuploidy. *Nat Rev Genet* **2**: 280-91.

Hayashi, K., K. Yoshida, and Y. Matsui. 2005. A histone H3 methyltransferase controls epigenetic events required for meiotic prophase. *Nature* **438**: 374-8.

Holloway, J.K., X.F. Sun, R. Yokoo, A.M. Villeneuve, and P.E. Cohen. 2014. Mammalian CNTD1 is critical for meiotic crossover maturation and deselection of excess precrossover sites. *Journal of Cell Biology* **205**: 633-641.

Hunter, N. 2015. Meiotic Recombination: The Essence of Heredity. *Cold Spring Harb Perspect Biol* **7**.

Hunter, N. and N. Kleckner. 2001. The single-end invasion: an asymmetric intermediate at the double-strand break to double-holliday junction transition of meiotic recombination. *Cell* **106**: 59-70.

Imai, Y., F. Baudat, M. Taillepierre, M. Stanzione, A. Toth, and B. de Massy. 2017. The PRDM9 KRAB domain is required for meiosis and involved in protein interactions. *Chromosoma*.

Inagaki, A., S. Schoenmakers, and W.M. Baarends. 2010. DNA double strand break repair, chromosome synapsis and transcriptional silencing in meiosis. *Epigenetics* **5**: 255-66.

Ishiguro, K., J. Kim, S. Fujiyama-Nakamura, S. Kato, and Y. Watanabe. 2011. A new meiosis-specific cohesin complex implicated in the cohesin code for homologous pairing. *EMBO Rep* **12**: 267-75.

Jee, J., J. Rozowsky, K.Y. Yip, L. Lochovsky, R. Bjornson, G. Zhong, Z. Zhang, Y. Fu, J. Wang, Z. Weng, and M. Gerstein. 2011. ACT: aggregation and correlation toolbox for analyses of genome tracks. *Bioinformatics* **27**: 1152-4.

Kauppi, L., M. Barchi, J. Lange, F. Baudat, M. Jasin, and S. Keeney. 2013. Numerical constraints and feedback control of double-strand breaks in mouse meiosis. *Genes Dev* **27**: 873-86.

Keeney, S., C.N. Giroux, and N. Kleckner. 1997. Meiosis-specific DNA double-strand breaks are catalyzed by Spo11, a member of a widely conserved protein family. *Cell* **88**: 375-84.

Khil, P.P., F. Smagulova, K.M. Brick, R.D. Camerini-Otero, and G.V. Petukhova. 2012. Sensitive mapping of recombination hotspots using sequencing-based detection of ssDNA. *Genome Res* **22**: 957-65.

Kleckner, N. 1996. Meiosis: How could it work? *Proceedings of the National Academy of Sciences of the United States of America* **93**: 8167-8174.

Kneitz, B., P.E. Cohen, E. Avdievich, L.Y. Zhu, M.F. Kane, H. Hou, R.D. Kolodner, R. Kucherlapati, J.W. Pollard, and W. Edelmann. 2000. MutS homolog 4 localization to meiotic chromosomes is required for chromosome pairing during meiosis in male and female mice. *Genes & Development* **14**: 1085-1097.

Koehler, K.E., J.P. Cherry, A. Lynn, P.A. Hunt, and T.J. Hassold. 2002. Genetic control of mammalian meiotic recombination. I. Variation in exchange frequencies among males from inbred mouse strains. *Genetics* **162**: 297-306.

Kohler, S., M. Wojcik, K. Xu, and A.F. Dernburg. 2017. Superresolution microscopy reveals the three-dimensional organization of meiotic chromosome axes in intact Caenorhabditis elegans tissue. *Proc Natl Acad Sci U S A* **114**: E4734-E4743.

Kugou, K., T. Fukuda, S. Yamada, M. Ito, H. Sasanuma, S. Mori, Y. Katou, T. Itoh, K. Matsumoto, T. Shibata, K. Shirahige, and K. Ohta. 2009. Rec8 guides canonical Spo11 distribution along yeast meiotic chromosomes. *Mol Biol Cell* **20**: 3064-76.

Kumar, R., N. Ghyselinck, K. Ishiguro, Y. Watanabe, A. Kouznetsova, C. Hoog, E. Strong, J. Schimenti, K. Daniel, A. Toth, and B. de Massy. 2015. MEI4 - a central player in the regulation of meiotic DNA double-strand break formation in the mouse. *J Cell Sci* **128**: 1800-11.

Lee, J., T. Iwai, T. Yokota, and M. Yamashita. 2003. Temporally and spatially selective loss of Rec8 protein from meiotic chromosomes during mammalian meiosis. *J Cell Sci* **116**: 2781-90.

Li, H., W. Watford, C. Li, A. Parmelee, M.A. Bryant, C. Deng, J. O'Shea, and S.B. Lee. 2007. Ewing sarcoma gene EWS is essential for meiosis and B lymphocyte development. *J Clin Invest* **117**: 1314-23.

Liu, E.Y., A.P. Morgan, E.J. Chesler, W. Wang, G.A. Churchill, and F. Pardo-Manuel de Villena. 2014. High-resolution sex-specific linkage maps of the mouse reveal polarized distribution of crossovers in male germline. *Genetics* **197**: 91-106.

Lynn, A., K.E. Koehler, L. Judis, E.R. Chan, J.P. Cherry, S. Schwartz, A. Seftel, P.A. Hunt, and T.J. Hassold. 2002. Covariation of synaptonemal complex length and mammalian meiotic exchange rates. *Science* **296**: 2222-5.

Mahadevaiah, S.K., J.M. Turner, F. Baudat, E.P. Rogakou, P. de Boer, J. Blanco-Rodriguez, M. Jasin, S. Keeney, W.M. Bonner, and P.S. Burgoyne. 2001. Recombinational DNA double-strand breaks in mice precede synapsis. *Nat Genet* **27**: 271-6.

Martini, E., V. Borde, M. Legendre, S. Audic, B. Regnault, G. Soubigou, B. Dujon, and B. Llorente. 2011. Genome-wide analysis of heteroduplex DNA in mismatch repair-deficient yeast cells reveals novel properties of meiotic recombination pathways. *PLoS Genet* **7**: e1002305.

Mulligan, P., T.F. Westbrook, M. Ottinger, N. Pavlova, B. Chang, E. Macia, Y.J. Shi, J. Barretina, J. Liu, P.M. Howley, S.J. Elledge, and Y. Shi. 2008. CDYL bridges REST and histone methyltransferases for gene repression and suppression of cellular transformation. *Mol Cell* **32**: 718-26.

Myers, S., R. Bowden, A. Tumian, R.E. Bontrop, C. Freeman, T.S. MacFie, G. McVean, and P. Donnelly. 2010. Drive against hotspot motifs in primates implicates the PRDM9 gene in meiotic recombination. *Science* **327**: 876-9.

Paigen, K., J.P. Szatkiewicz, K. Sawyer, N. Leahy, E.D. Parvanov, S.H. Ng, J.H. Graber, K.W. Broman, and P.M. Petkov. 2008. The recombinational anatomy of a mouse chromosome. *PLoS Genet* **4**: e1000119.

Parvanov, E.D., P.M. Petkov, and K. Paigen. 2010. Prdm9 controls activation of mammalian recombination hotspots. *Science* **327**: 835.

Parvanov, E.D., H. Tian, T. Billings, R.L. Saxl, C. Spruce, R. Aithal, L. Krejci, K. Paigen, and P.M. Petkov. 2017. PRDM9 interactions with other proteins provide a link between recombination hotspots and the chromosomal axis in meiosis. *Mol Biol Cell* **28**: 488-499.

Patel, A., J.R. Horton, G.G. Wilson, X. Zhang, and X. Cheng. 2016. Structural basis for human PRDM9 action at recombination hot spots. *Genes Dev* **30**: 257-65.

Peters, A.H., A.W. Plug, M.J. van Vugt, and P. de Boer. 1997. A drying-down technique for the spreading of mammalian meiocytes from the male and female germline. *Chromosome Res* **5**: 66-8.

Petkov, P.M., K.W. Broman, J.P. Szatkiewicz, and K. Paigen. 2007. Crossover interference underlies sex differences in recombination rates. *Trends Genet* **23**: 539-42.

Powers, N.R., E.D. Parvanov, C.L. Baker, M. Walker, P.M. Petkov, and K. Paigen. 2016. The Meiotic Recombination Activator PRDM9 Trimethylates Both H3K36 and H3K4 at Recombination Hotspots In Vivo. *PLoS Genet* **12**: e1006146.

Reynolds, A., H.Y. Qiao, Y. Yang, J.K. Chen, N. Jackson, K. Biswas, J.K. Holloway, F. Baudat, B. de Massy, J. Wang, C. Hoog, P.E. Cohen, and N. Hunter. 2013. RNF212 is a dosage-sensitive regulator of crossing-over during mammalian meiosis. *Nature Genetics* **45**: 269-278.

Robert, T., A. Nore, C. Brun, C. Maffre, B. Crimi, H.M. Bourbon, and B. de Massy. 2016. The TopoVIB-Like protein family is required for meiotic DNA double-strand break formation. *Science* **351**: 943-949.

Romanienko, P.J. and R.D. Camerini-Otero. 1999. Cloning, characterization, and localization of mouse and human SPO11. *Genomics* **61**: 156-69.

Schwartz, J.C., T.R. Cech, and R.R. Parker. 2015. Biochemical Properties and Biological Functions of FET Proteins. *Annu Rev Biochem* **84**: 355-79.

Smagulova, F., I.V. Gregoretti, K. Brick, P. Khil, R.D. Camerini-Otero, and G.V. Petukhova. 2011. Genome-wide analysis reveals novel molecular features of mouse recombination hotspots. *Nature* **472**: 375-8.

Stanzione, M., M. Baumann, F. Papanikos, I. Dereli, J. Lange, A. Ramlal, D. Trankner, H. Shibuya, B. de Massy, Y. Watanabe, M. Jasin, S. Keeney, and A. Toth. 2016. Meiotic DNA break formation requires the unsynapsed chromosome axis-binding protein IHO1 (CCDC36) in mice. *Nat Cell Biol* **18**: 1208-1220.

Sun, F., Y. Fujiwara, L.G. Reinholdt, J. Hu, R.L. Saxl, C.L. Baker, P.M. Petkov, K. Paigen, and M.A. Handel. 2015. Nuclear localization of PRDM9 and its role in meiotic chromatin modifications and homologous synapsis. *Chromosoma*.

Tang, S., M.K. Wu, R. Zhang, and N. Hunter. 2015. Pervasive and essential roles of the Top3-Rmi1 decatenase orchestrate recombination and facilitate chromosome segregation in meiosis. *Mol Cell* **57**: 607-21.

Tate, C.M., J.H. Lee, and D.G. Skalnik. 2010. CXXC finger protein 1 restricts the Setd1A histone H3K4 methyltransferase complex to euchromatin. *FEBS J* **277**: 210-23.

Tian, H., T. Billings, and P.M. Petkov. 2018. CXXC1 is redundant for normal DNA double-strand break formation and meiotic recombination in mouse. *BIORXIV preprint server*.

Walker, M., T. Billings, C.L. Baker, N. Powers, H. Tian, R.L. Saxl, K. Choi, M.A. Hibbs, G.W. Carter, M.A. Handel, K. Paigen, and P.M. Petkov. 2015. Affinity-seq detects genome-wide PRDM9 binding sites and reveals the impact of prior chromatin modifications on mammalian recombination hotspot usage. *Epigenetics Chromatin* **8**: 31.

Wang, S., T. Hassold, P. Hunt, M.A. White, D. Zickler, N. Kleckner, and L. Zhang. 2017. Inefficient Crossover Maturation Underlies Elevated Aneuploidy in Human Female Meiosis. *Cell*.

Ward, A., J. Hopkins, M. McKay, S. Murray, and P.W. Jordan. 2016. Genetic Interactions Between the Meiosis-Specific Cohesin Components, STAG3, REC8, and RAD21L. *G3 (Bethesda)* **6**: 1713-24.

Xu, H., M.D. Beasley, W.D. Warren, G.T. van der Horst, and M.J. McKay. 2005. Absence of mouse REC8 cohesin promotes synapsis of sister chromatids in meiosis. *Dev Cell* **8**: 949-61.

Yoon, S.W., M.S. Lee, M. Xaver, L. Zhang, S.G. Hong, Y.J. Kong, H.R. Cho, N. Kleckner, and K.P. Kim. 2016. Meiotic prophase roles of Rec8 in crossover recombination and chromosome structure. *Nucleic Acids Res* **44**: 9296-9314.

Tian_Fig1

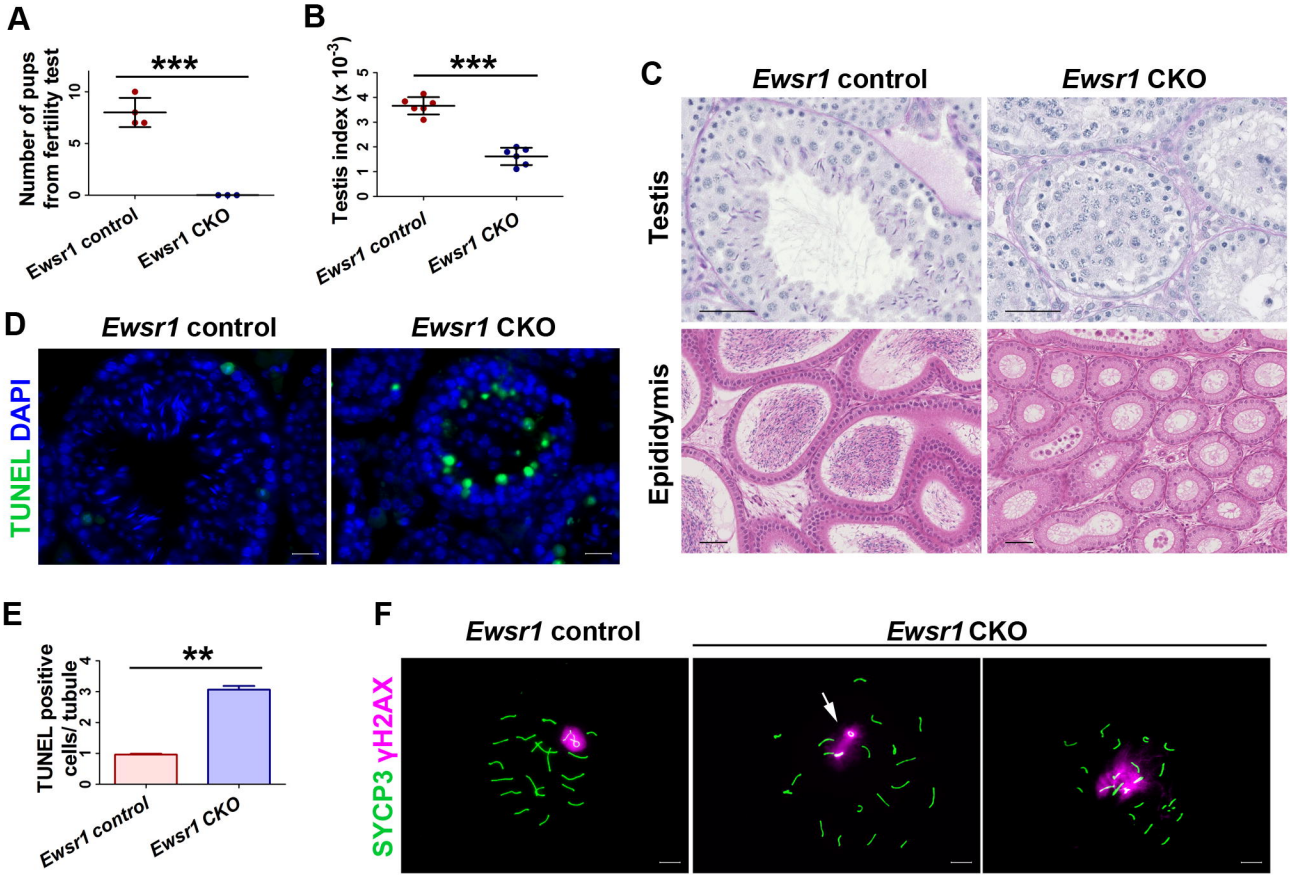
A
Number of pups from fertility test
***
Ewsr1 control
Ewsr1 CKO
B
Testis index (x 10-3)
***
Ewsr1 control
Ewsr1 CKO
C
Ewsr1 control
Ewsr1 CKO
Testis
Epididymis
D
Ewsr1 control
Ewsr1 CKO
TUNEL DAPI
E
TUNEL positive cells/ tubule
**
Ewsr1 control
Ewsr1 CKO
F
Ewsr1 control
Ewsr1 CKO
SYCP3 γH2AX

Tian_Fig2

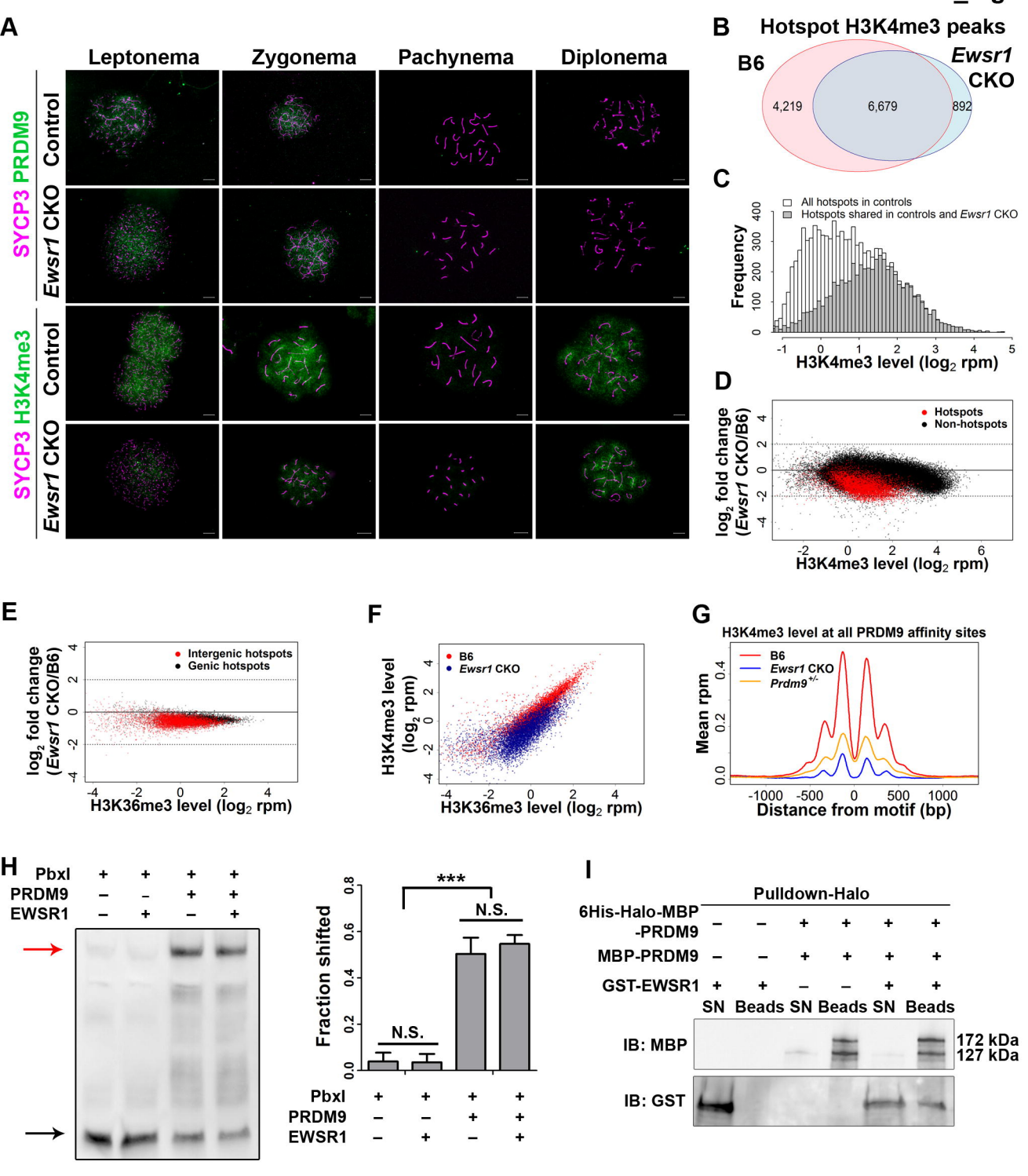
A
Leptonema
Zygonema
Pachynema
Diplonema
SYCP3 PRDM9
Control
Ewsr1 CKO
SYCP3 H3K4me3
Control
Ewsr1 CKO
B
Hotspot H3K4me3 peaks
B6
Ewsr1 CKO
4,219
6,679
892
C
All hotspots in controls
Hotspots shared in controls and Ewsr1 CKO
Frequency
H3K4me3 level (log2 rpm)
D
Hotspots
Non-hotspots
log2 fold change (Ewsr1 CKO/B6)
H3K4me3 level (log2 rpm)
E
Intergenic hotspots
Genic hotspots
log2 fold change (Ewsr1 CKO/B6)
H3K36me3 level (log2 rpm)
F
B6
Ewsr1 CKO
H3K4me3 level (log2 rpm)
H3K36me3 level (log2 rpm)
G
H3K4me3 level at all PRDM9 affinity sites
B6
Ewsr1 CKO
Prdm9+/-
Mean rpm
Distance from motif (bp)
H
PbxI
PRDM9
EWSR1
Fraction shifted
***
N.S.
N.S.
I
Pulldown-Halo
6His-Halo-MBP-PRDM9
MBP-PRDM9
GST-EWSR1
SN
Beads
IB: MBP
IB: GST
172 kDa
127 kDa

Tian_Fig3

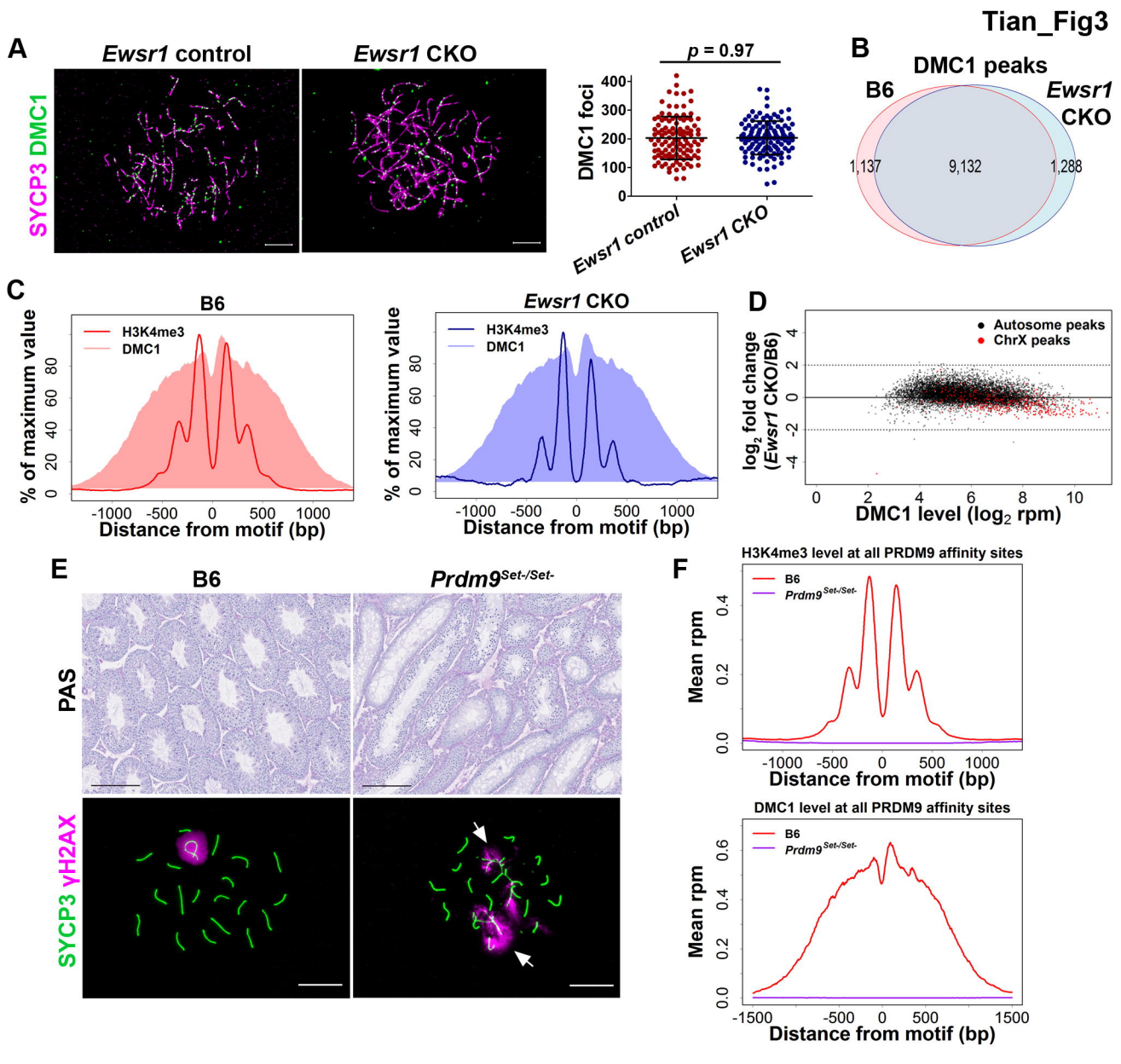
A
Ewsr1 control
Ewsr1 CKO
SYCP3 DMC1
p = 0.97
DMC1 foci
400
300
200
100
0
Ewsr1 control
Ewsr1 CKO
B
DMC1 peaks
B6
Ewsr1 CKO
1,137
9,132
1,288
C
B6
H3K4me3
DMC1
% of maximum value
0 20 40 60 80
-1000 -500 0 500 1000
Distance from motif (bp)
Ewsr1 CKO
H3K4me3
DMC1
% of maximum value
0 20 40 60 80
-1000 -500 0 500 1000
Distance from motif (bp)
D
Autosome peaks
ChrX peaks
log2 fold change (Ewsr1 CKO/B6)
4 2 0 -2 -4
0 2 4 6 8 10
DMC1 level (log2 rpm)
E
B6
Prdm9Set-/Set-
PAS
SYCP3 γH2AX
F
H3K4me3 level at all PRDM9 affinity sites
B6
Prdm9Set-/Set-
Mean rpm
0.0 0.2 0.4
-1000 -500 0 500 1000
Distance from motif (bp)
DMC1 level at all PRDM9 affinity sites
B6
Prdm9Set-/Set-
Mean rpm
0.0 0.2 0.4 0.6
-1500 -500 0 500 1500
Distance from motif (bp)

Tian_Fig4

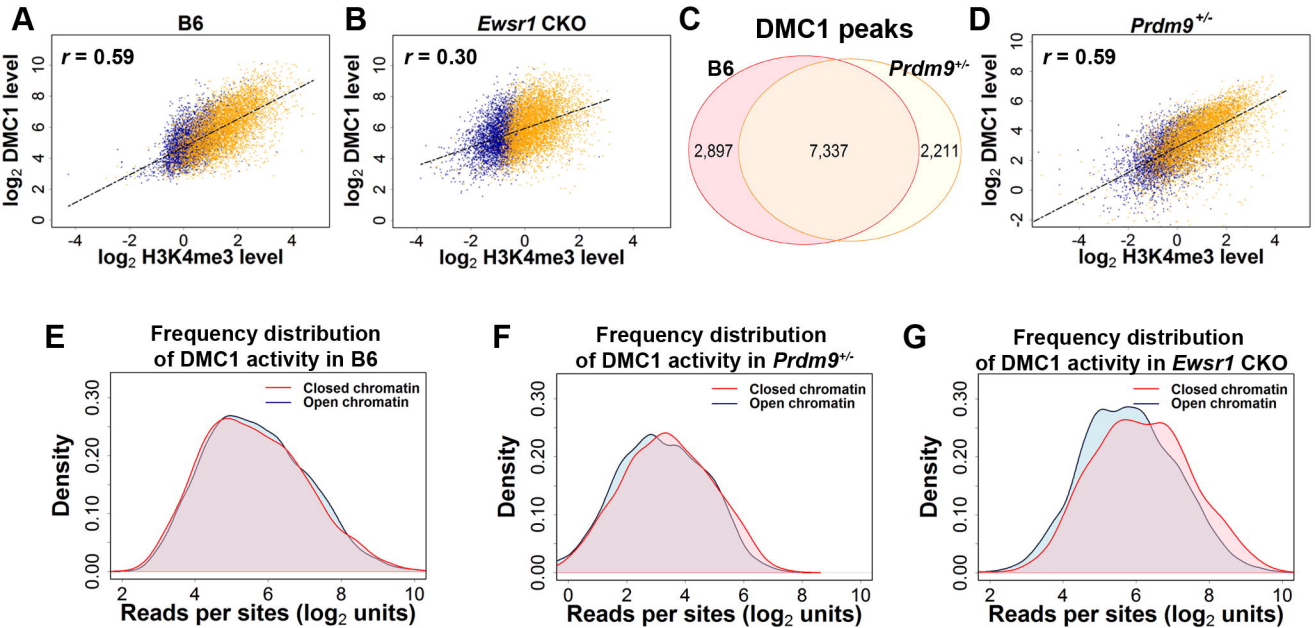
A
B6
r = 0.59
log2 DMC1 level
log2 H3K4me3 level
B
Ewsr1 CKO
r = 0.30
log2 DMC1 level
log2 H3K4me3 level
C
DMC1 peaks
B6
Prdm9+/-
2,897
7,337
2,211
D
Prdm9+/-
r = 0.59
log2 DMC1 level
log2 H3K4me3 level
E
Frequency distribution of DMC1 activity in B6
Closed chromatin
Open chromatin
Density
Reads per sites (log2 units)
F
Frequency distribution of DMC1 activity in Prdm9+/-
Closed chromatin
Open chromatin
Density
Reads per sites (log2 units)
G
Frequency distribution of DMC1 activity in Ewsr1 CKO
Closed chromatin
Open chromatin
Density
Reads per sites (log2 units)

Tian_Fig5

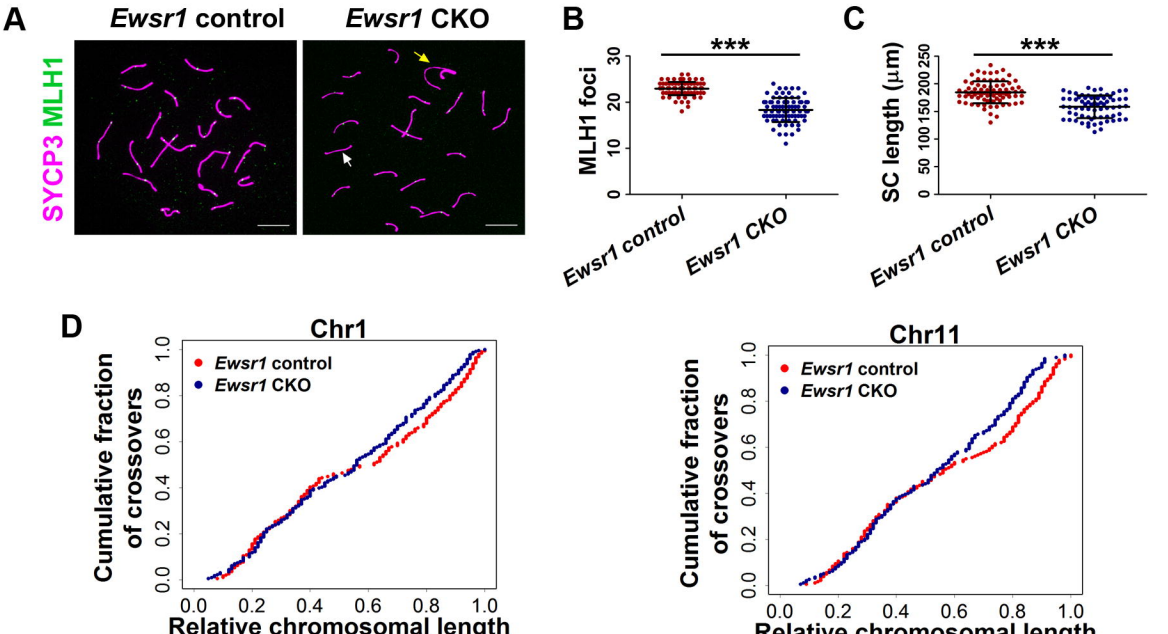
A
Ewsr1 control
Ewsr1 CKO
SYCP3 MLH1
B
MLH1 foci
***
Ewsr1 control
Ewsr1 CKO
C
SC length (μm)
***
Ewsr1 control
Ewsr1 CKO
D
Chr1
Ewsr1 control
Ewsr1 CKO
Cumulative fraction of crossovers
Relative chromosomal length
Chr11
Ewsr1 control
Ewsr1 CKO
Cumulative fraction of crossovers
Relative chromosomal length

Tian_Fig6

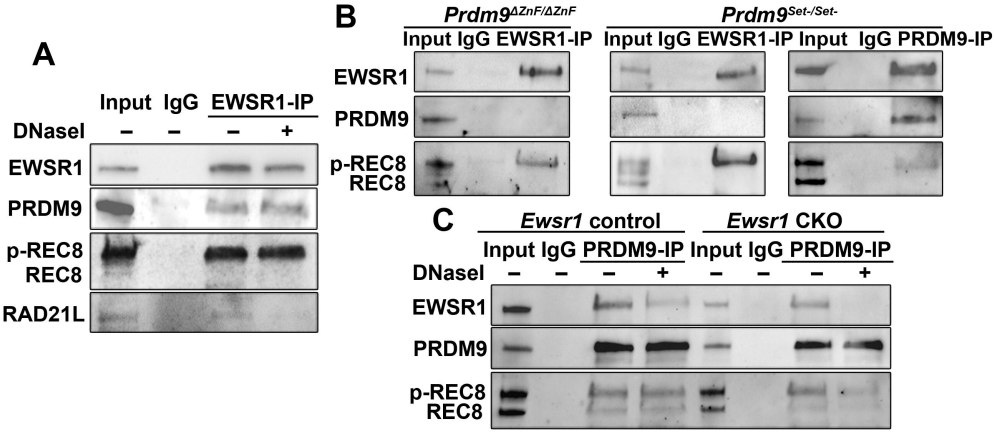
A
Input
IgG
EWSR1-IP
DNaseI
–
–
–
+
EWSR1
PRDM9
p-REC8
REC8
RAD21L
B
Prdm9ΔZnF/ΔZnF
Prdm9Set-/Set-
Input IgG EWSR1-IP
Input IgG EWSR1-IP
Input IgG PRDM9-IP
EWSR1
PRDM9
p-REC8
REC8
C
Ewsr1 control
Ewsr1 CKO
Input IgG PRDM9-IP
Input IgG PRDM9-IP
DNaseI
– – – + – – – +
EWSR1
PRDM9
p-REC8
REC8

Tian_Fig7

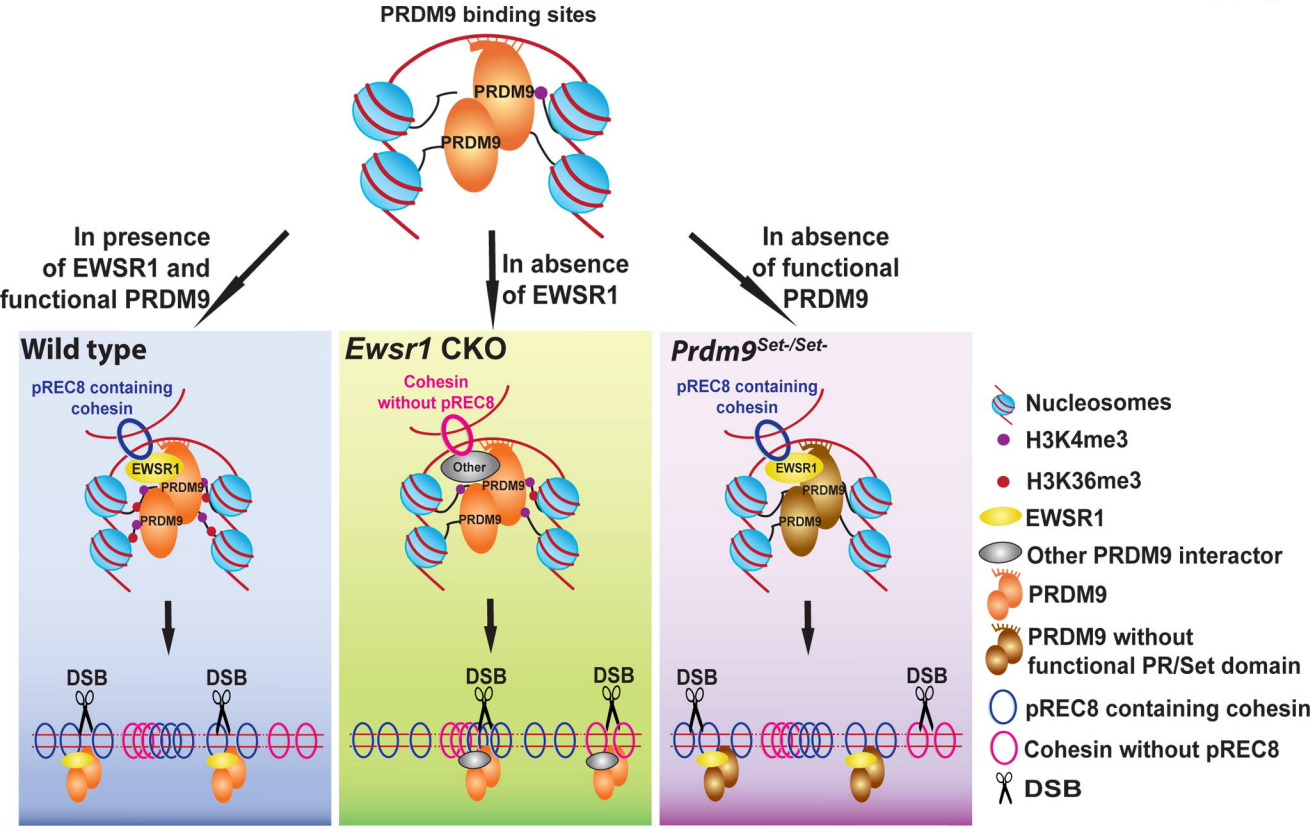
PRDM9 binding sites
PRDM9
PRDM9
In presence of EWSR1 and functional PRDM9
In absence of EWSR1
In absence of functional PRDM9
Wild type
pREC8 containing cohesin
EWSR1
PRDM9
PRDM9
DSB
DSB
Ewsr1 CKO
Cohesin without pREC8
Other
PRDM9
PRDM9
DSB
DSB
Prdm9Set-/Set-
pREC8 containing cohesin
EWSR1
PRDM9
PRDM9
DSB
DSB
Nucleosomes
H3K4me3
H3K36me3
EWSR1
Other PRDM9 interactor
PRDM9
PRDM9 without functional PR/Set domain
pREC8 containing cohesin
Cohesin without pREC8
DSB